Improving the Corrosion Resistance of Ni/SS Thin Films by Nitrogen Ion Implantation

A. Grayeli Korpi[a], A. Arman[b], S. Jurečka[c], C. Luna[d], R. Shakoury[e], Ş. Ţălu[f], S. Rezaee[g,*], K. Ghosh[h], K. Sherafat[b], M. Sadeghi[i] and S. Gopikishan[j]

[a]Physics and Accelerators Research School, Nuclear Sciences and Technology Research Institute, Tehran, Iran
[b]Vacuum Technology Research Group, ACECR, Sharif University Branch, Tehran, Iran
[c] University of Žilina, Faculty of Electrical Engineering, Institute of Aurel Stodola, Nálepku 1390, 031 01 Liptovský Mikuláš, Slovakia
[d] Universidad Autónoma de Nuevo León (UANL), Facultad de Ciencias Físico Matemáticas (FCFM), Av. Universidad s/n, San Nicolás de los Garza, 66455, Nuevo León, Mexico
[e]Department of Physics, Faculty of Science, Imam Khomeini International University, Qazvin, Iran
[f]Technical University of Cluj-Napoca, The Directorate of Research, Development and Innovation Management (DMCDI), Constantin Daicoviciu Str., no. 15, Cluj-Napoca, 400020, Cluj county, Romania
[g]Department of Physics, Kermanshah Branch, Islamic Azad University, Kermanshah, Iran
[h] Department of Pure and Applied Physics, Guru Ghasidas Vishwavidyalaya, Bilaspur-495009, Chhattisgarh, India
[i]Institute of Technology Development, ACECR, Sharif University Branch, Tehran, Iran
[j]Institute of Aeronautical Engineering, Department of Physics, Hyderabad, Telangana, India

(Received July 17, 2019; revised version July 29, 2019; in final form July 30, 2019)

N^+ ions were incorporated into nickel-coated 316 stainless steel (SS) at room temperature using different energies (10, 20, and 50 keV) and a fluence of 5×10^{17} N^+ cm^{-2}. The microstructure, surface morphology, and corrosion inhibition of the obtained materials were investigated and compared with the properties of the untreated steel using several analytical techniques. The X-ray diffraction patterns indicated the formation of nickel nitride with the ion implantation process. The surface morphology of the samples was studied by atomic force microscopy and statistical and multifractal analytical methods. Moreover, the potentiodynamic polarization test in 3.5% NaCl solution was carried out to evaluate the corrosion properties of the samples. These studies revealed that the generalized fractal dimension, D_q, is dependent on the ion implantation energy and the symmetry of the multifractal singularity spectra, $f(\alpha)$, which is related to the uniformity of the sample. In this manner, the lowest value was obtained for the sample prepared with the maximum ion implantation energy. Also, the increment of the implantation energy yields to increase the corrosion resistance. The simultaneous decrease of the corrosion current density (I_{corr}) and the increase of the corrosion potential observed with the N^+ ion-implantation indicate that treated samples are more resistant to corrosion than the untreated steel, and the highest corrosion protection was observed for the maximum implantation energy (50 keV). The correlation between corrosion resistance, structural and surface morphology induced by implantation is discussed.

DOI: 10.12693/APhysPolA.136.536

PACS/topics: ion implantation, Ni/SS, corrosion, micromorphology, AFM, polarization

1. Introduction

Ion implantation is a surface modification method to produce new materials by impingement of high-energy ions from an ion accelerator in the specimen's surface. This process modifies the mechanical, optical, and structural properties of the initial material. An electric field accelerates the ions to bombard the target. The energy of the accelerated ions, modulated with the electric field, is the implantation energy and its values are in the range from electron volts to mega-electron volts. The target material properties are changed according to the nature, quantity, and energy of the ions providing various applications [1–5].

The hardness and corrosion resistance of the target is improved via the interaction between the implanted ions and target [3, 5]. Among the advantages of this surface modification method, it is emphasized that: (i) it does not need high temperatures, (ii) the implantation procedure has no effect on the bulk material and (iii) the sample surface can be finely tailored controlling the implantation parameters and the accelerating potential [6].

In this regard, the nitrogen ion implantation effect on the corrosion resistance of stainless steel has attracted considerable attention due to its technological and industrial implications [7–9].

*corresponding author; e-mail: Saharrezaee593@iauksh.ac.ir

Nitrogen implantation induces the formation of austenite, which increases the mechanical strength of steel, increasing the confinement of the steel corrosion [10]. A solid solution is obtained from the diffusion of nitrogen during the implantation in the structure of steel without chromium and iron nitride formations. Regarding the viewpoint of corrosion properties, the formation of chromium nitride is harmful [11, 12].

Many researchers have studied the effect of nitrogen ion implantation on the corrosion resistance of stainless steel [13–15]. However, further studies are required to determine well-defined synthesis conditions to improve the formation of the desirable nitride layer. On the other hand, the effect of the nitrogen ion implantation on the surface texture and the influence of the produced changes in the surface morphology on the corrosion resistance remains open to analysis. In this type of experiments, atomic force microscopy (AFM) is an indispensable tool to obtain experimental information about the surface roughness of samples. However, the suitable selection of the analysis method of the AFM data is crucial to extract the relevant information to characterize the morphology properties of surfaces. For this reason, a variety of approaches based on the use of functional characterizations and fractal analysis have been implemented during the last few years in the study of thin films [16–22].

The goal of the present research is to examine the influence of nitrogen ion implantation under different implantation energies on the surface roughness and corrosion properties of the nickel-coated 316 stainless steel films. The 3D surface microtexture of the samples was characterized by means of AFM measurements and the use of statistical and multi-fractal analytical methods. The correlation between the surface morphology of the samples and their corrosion properties in chloride media is studied.

2. Experimental details

Specimens with dimensions of $20 \times 20 \times 0.7$ mm^3 were cut from sheets of AISI 316 SS. These samples were subsequently cleaned by ultrasonication in heated acetone (CH_3COCH_3), and then with ethanol (C_2H_5OH). The deposition of nickel films (99.98% in purity) with thickness of 100 nm on SS substrates was carried out using the electron beam evaporation at room temperature with a deposition rate of 0.1 Å/s. A quartz crystal deposition rate controller (Sigma Instruments, SQM-160, USA) was used to control the film thickness. An electron beam evaporation coating plant (E19A3 Edwards, England) was used with a base pressure of 2×10^{-6} mbar. The ion implantation of the samples was performed by nitrogen at 400 K with a fluence of 5×10^{17} N^+ cm^{-2} and with three different energies: 10, 20, and 50 keV.

The crystalline structure of these films was determined using a STOE model STADI MP Diffractometer (Cu K_α radiation) with a step size of 0.02° and a count time of 1.0 s per step.

The surface morphology of N^+ implanted samples was characterized by AFM before the corrosion tests using a NT-MDT scanning probe microscope in semi-contact mode, using a Si tip of 10 nm in diameter.

A potentiodynamic method was used to study the electrochemical properties of the samples using a potentiostat coupled to a PC (EG&G273A). All electrochemical experiments were done in a 3.5 wt% NaCl solution at room temperature. The exposed surface area of the samples was 1.0 ± 0.05 cm^2. A platinum counter-electrode and a saturated calomel reference electrode (SCE) were used for the three-electrode setup. The samples were polarized from −600 mV versus open circuit potential at a scan rate of 1 mV s^{-1}. All the potentials presented in this work are referenced to SCE.

3. Results and discussion

3.1. XRD results

Figure 1 shows the XRD pattern of the bare stainless steel substrate and the nitrogen implanted Ni/SS (316) samples obtained with a fluence of 5×10^{17} N^+ cm^{-2} at 400 K temperature and different implantation energies (10, 20, and 50 keV).

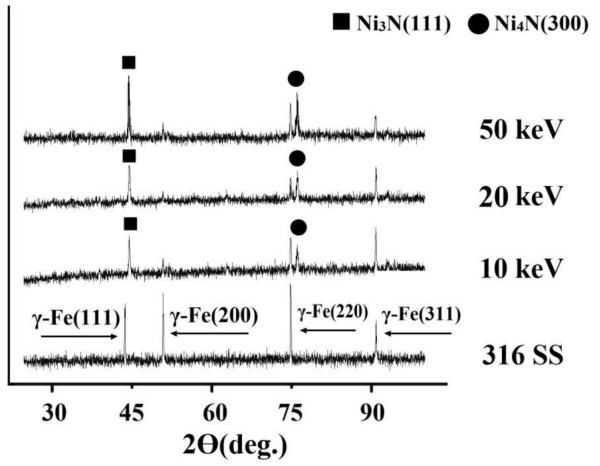

Fig. 1. XRD patterns of AISI 316 SS and N^+ ion-implanted samples with different nitrogen ion energies (10, 20, and 50 keV).

The XRD pattern of bare stainless steel sample displays the presence of austenite peaks around $2\theta = 43.71°$, 50.78°, 74.81°, and 90.08°, corresponding to the reflections of γ-Fe(111), γ-Fe(200), γ-Fe(220) and γ-Fe(311) planes, respectively.

The XRD patterns of the ion-implanted samples with different energies at the same dose of 5×10^{17} N^+ cm^{-2} and at 400 K, show two peaks at $2\theta = 44.48°$ and $2\theta = 76.08°$ that can be assigned to the (111) and (300) crystallographic planes of Ni_3N (JCPDS Card No. 010-0280) and Ni_4N (JCPDS Card No. 36-1300), respectively.

It is clear that by increasing the implantation energy from 10 to 50 keV, the intensities of nickel nitride peaks, namely $Ni_3N(111)$ and $Ni_4N(300)$ are enhanced.

The intensities of the nickel nitride diffraction peaks are the highest for the sample obtained with implantation energy of 50 keV. Hence, the formation of nickel nitride crystallites is improved in this sample in comparison with samples fabricated with lower implantation energies. These changes in the intensity of the XRD peaks provide useful information to analyse the results obtained from the potentiodynamic tests.

The Scherrer formula is used to obtain the crystallite size, D (coherently diffracting domains) [23–27]:

$$B = \frac{k\lambda}{D\cos\theta}, \tag{1}$$

where B is the width of the diffraction peak, λ is the X-ray wavelength, θ is the Bragg angle, and k is a dimensionless constant relating to the shape and distribution of crystallites [28] (usually considered close to unity).

To determine the value for B [29] the standard measurement method is applied

$$B^2 = w_0^2 - w_i^2, \tag{2}$$

where w_0 is the full width at half-maximum (FWHM) of the films and w_i is the FWHM of the strain free samples.

TABLE I

Crystallite size and corrosion parameters of Ni/AISI 316 samples obtained at different implantation energies

Sample		Energy [keV]	D_{XRD} [nm]	Corrosion current density [μA cm^{-2}]	Corrosion potential (V vs. SCE)
bare 316 SS		–	–	19.49	−0.51
implanted samples	(a)	10	20.1	2.95	−0.31
	(b)	20	32.6	0.79	−0.17
	(c)	50	77.4	0.03	−0.13

Table I depicts the variation of the crystallite size, D (coherently diffracting domains) calculated from the $Ni_3N(111)$ peak as a function of energy implantation [21]. It is well known that the size of the particles depends on implantation energy [25] and the crystallinity is improved upon heat treatments [27, 30]. From data of Table I, it is observed that the crystallite size increases with the implantation energy.

3.2. AFM results

Figure 2 shows AFM images of scanned areas of 5.0×5.0 μm^2 of the different samples. The root mean square (RMS) roughness and peak-to-peak values determined from observed AFM surface height function are presented in Table II.

TABLE II

RMS roughness and peak-to-peak values determined from the AFM images (in nm units).

Sample	Energy [keV]	RMS roughness [nm]	Peak-to-peak value [nm]
(a)	10	13.60	107.38
(b)	20	11.49	78.68
(c)	50	13.39	115.25

These results indicate that the nitrogen ion implantation strongly influences on the sample surface morphology. The RMS roughness is reduced when the ion implantation energy is increased from 10 keV to 20 keV, and it increases again when the implantation energy is increased up to 50 keV. This trend is also observed for the peak-to-peak value, finding the highest value for the sample treated with the maximum ion implantation energy (50 keV).

The surface morphology described by the random height function is developed dynamically with the implantation energy. The high non-uniformity of the random height function often possesses rich scaling and self-similarity properties [31–35], and the multifractal formalism can accurately describe them. Multifractal methods describe the morphology properties in terms of the multifractal singularity spectrum $f(\alpha)$ and generalized fractal dimension D_q [36, 37].

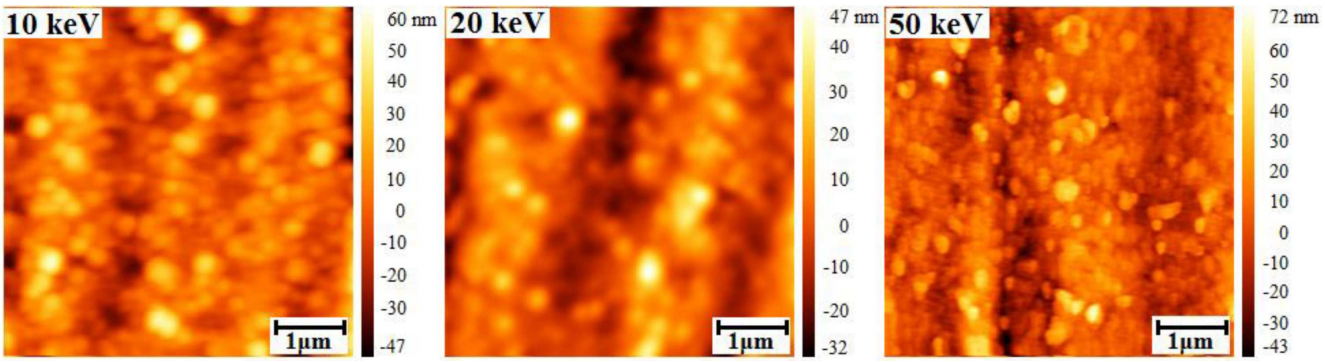

Fig. 2. The AFM images of implanted samples with different nitrogen ion energies of 10, 20, and 50 keV.

In this work, the computations of the $f(\alpha)$ and D_q values are based on an algorithm developed by Chhabra et al. [38].

The multi-fractal singularity spectra $f(\alpha)$ for the treated samples with implantation energies of 10, 20, and 50 keV are shown in Fig. 3. The $f(\alpha)$ curves have concave shapes, which is a typical characteristic of the multi-fractal surface morphology. Therefore, the three samples show well-developed multi-fractal properties.

The maximum height D_0 and the width of the $f(\alpha)$ curve directly correspond to the shape variability of the morphological objects. From Fig. 3 we can conclude that the variability of the morphological objects increases for 10 keV and 20 keV energies and then drastically decreases for the implantation energy of 50 keV. The symmetry of the $f(\alpha)$ curves are different for all observed surfaces indicating the degree of non-uniformity. The highest non-uniformity is observed for the implantation energy of 20 keV and the lowest corresponds to the energy of 50 keV.

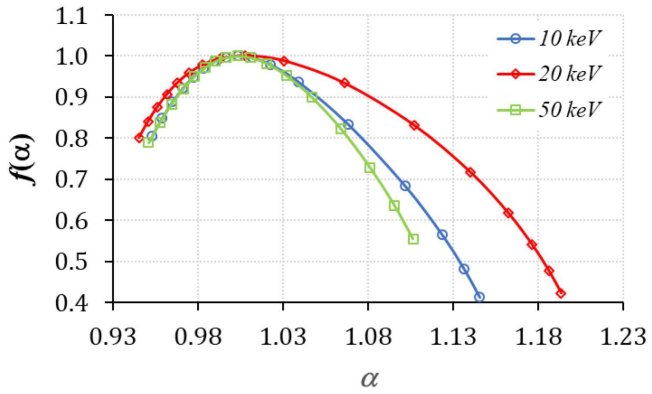

Fig. 3. The multi-fractal singularity spectra $f(\alpha)$ of implanted samples with different nitrogen ion implantation energies (10, 20 and 50 keV).

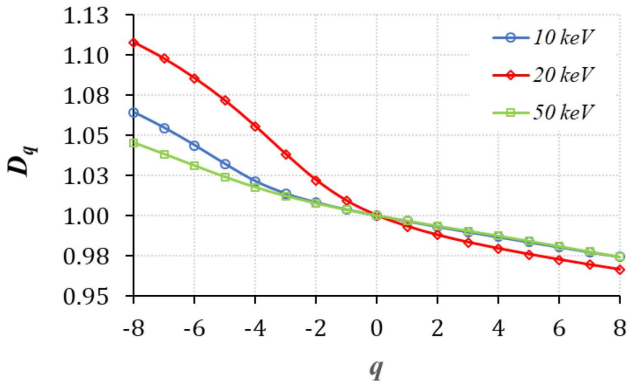

Fig. 4. The generalized fractal dimension D_q of implanted samples with different nitrogen ion energies of 10, 20, and 50 keV.

Generalized fractal dimensions D_q are shown in Fig. 4. The shapes of the D_q curves are typical for multi-fractal surface morphology showing an inflection point. Multi-fractal properties of observed surface morphology are enhanced for the structure treated at 20 keV, and significantly decrease when the nitrogen implantation energy is 50 keV. In the last case, surface morphology changes substantially. The correlation dimension for $q \geq 2$ has the lowest values for the film treated with an implantation energy of 20 keV, which is related with the most moderated degree of surface homogeneity.

3.3. Polarization results

Figure 5 shows the potentiodynamic polarization curves of the untreated and the nitrogen implanted Ni coated 316 stainless steel with different ion implantation energies (10, 20, and 50 keV) in 3.5% NaCl solution. None of these samples have shown active-passive behavior. Also, the polarization plots reveal that the deposition of nickel and nitrogen ion implantation increases the resistance of the stainless steel against corrosive media. A remarkable tendency to corrosion protection for the treated SS samples, with the polarization curves shifting towards lower corrosion current densities and higher corrosion potentials, can be observed in Fig. 5.

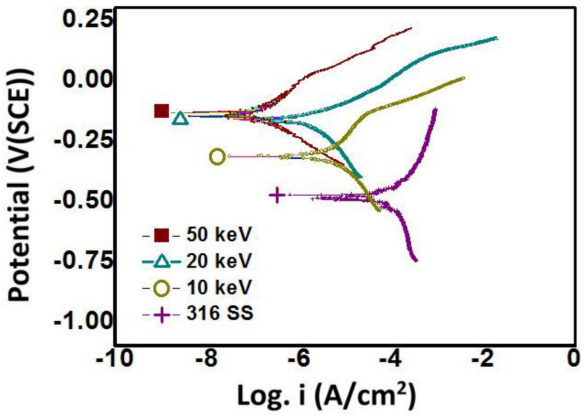

Fig. 5. Polarization curves obtained for AISI 316 SS and implanted samples with nitrogen ion energies of 10, 20, and 50 keV using NaCl (3.5%) solution as the corroding environment at room temperature.

The optimum corrosion current density and corrosion potential are obtained at 0.03 μA/cm^2 and -0.13 V, respectively, for sample implanted with 50 keV versus SCE, while these quantities for bare AISI 316 substrate are 19.49 μA/cm^2 and -0.51 V versus SCE, respectively.

Table I gives information about the quantitative values of the corrosion-related parameters resulted from the polarization plots.

3.4. Discussion

In the present work, the relationship between surface multi-affinity and corrosion property of the Ni coated 316

stainless steel has been investigated with different nitrogen ion implantation energies of 10, 20, and 50 keV in 3.5% NaCl solution. Figure 3 shows that in the 10 keV and 20 keV samples vertical complexity (Δf) of the surfaces almost do not change ($\Delta f = 0.4$) and the spatial complexity ($\Delta\alpha$) increases with increasing ion energy from 10 keV ($\Delta\alpha = 0.19$) to 20 keV ($\Delta\alpha = 0.25$). On the other hand, the anti-corrosion behaviour is improved with the ion implantation which may be due to the nitridation of the surface. After increasing the ion implantation energy to 50 keV, both the vertical and spatial complexity decreases and accordingly, the corrosion resistance improves. The multi-fractal spectra of implanted samples show that spatial complexity has almost no effect, but the vertical complexity has a significant effect on corrosion behaviour. A vertically rough surface contains many hillocks and they may act as electrodes. Thus, the presence of a larger number of microelectrodes in the vertically more complex microstructure of the samples makes them more prone to corrosion [39]. Thus multi-fractal spectra could become a new way to analyse the correlation among multi-affinity of a surface and corrosion behaviour. It seems that the improvement of the corrosion resistance with increasing ion energy is due to the combined effects of surface quality enhancement and nitridation of the samples.

4. Conclusions

In the present study, it has been shown that nickel coating and nitrogen ion implantation have a dominant effect on corrosion protection of 316 austenitic stainless steel.

The XRD characterization reveals the formation of nickel nitride after the ion implantation, and the maximum intensity of nickel nitride peaks belongs to the sample implanted at higher energy (50 keV). This sample exhibits the highest corrosion resistance, and it is related to the formation of nickel nitride.

Statistical and multi-fractal analyses of the surface height function obtained from the AFM experiments provide information about the development of the surface morphology with the energy of nitrogen implantation. Generalized fractal dimension and multi-fractal singularity spectra show results consistent with the XRD and polarization analyses.

The surface morphology of the sample implanted at 50 keV show different properties that are suitable for the explanation of the highest surface corrosion resistance.

References

[1] P. Saravanan, V.S. Raja, S. Mukherjee, *Surf. Coat. Technol.* **201**, 8131 (2007.

[2] M. Oikawa, T. Kamiya, M. Fukuda, S. Okumura, H. Inoue, S. Masuno, S. Umemiya, Y. Oshiyama, Y. Taira, *Nucl. Instrum. Methods Phys. Res. B* **210**, 54 (2003).

[3] W. Wang, J.H. Booske, C. Baum, C. Clothier, N. Zjaba, L. Zhang, *Surf. Coat. Technol.* **111**, 97 (1999).

[4] A.A. Zavarian, Ş. Ţălu, F. Hafezi, A. Achour, C. Luna, S. Naderi, M. Mardani, A. Arman, A. Ahmadpourian, *J. Mater. Sci. Mater. Electron.* **28**, 15293 (2017).

[5] A. Fossati, F. Borgioli, E. Galvanetto, T. Bacci, *Surf. Coat. Technol.* **200**, 3511 (2006).

[6] S. Fayeulle, *Def. Diff. Forum* **57**, 372 (1988).

[7] R.F.A. Jargelius-Pettersso, *Corros. Sci.* **41**, 1639 (1999).

[8] L. Liu, Y.Y. Sheng, M. Liu, M. Dienwiebel, Z. Zhang, D. Dastan, *Tribol. Int.* **140**, 105727 (2019).

[9] V. Singh, K. Marchev, C.V. Cooper, E.I. Meletis, *Surf. Coat. Technol.* **160**, 249 (2002).

[10] R.W. Revie, H.H. Uhlig, *Corrosion and Corrosion Control*, 3rd ed., Wiley-Interscience, 2008, p. 407.

[11] J.P. Riviere, P. Meheust, J.P. Villain, C. Templier, M. Cahoreau, G. Abrasonis, L. Pranevicius, *Surf. Coat. Technol.* **158**, 99 (2002).

[12] B. Chico, L. Martinez, F.J. Perez, *Appl. Surf. Sci.* **243**, 409 (2005).

[13] S. Fujimoto, H. Hayashida, T. Shibata, *Mater. Sci. Eng.* **A267**, 314 (1999).

[14] A.R. Grayeli-Korpi, H. Savaloni, *Appl. Surf. Sci.* **258**, 9982 (2012).

[15] H. Savaloni, M. Habibi, *Appl. Surf. Sci.* **258**, 103 (2011).

[16] K. Smagoń, S. Stach, Ş. Ţălu, A. Arman, A. Achour, C. Luna, N. Ghobadi, M. Mardani, F. Hafezi, A. Ahmadpourian, M. Ganji, A.G. Korpi, *Europ. Phys. J. Plus* **132**, 520 (2017).

[17] X.-T. Yin, W.-D. Zhou, J. Li, Q. Wang, F.-Y. Wu, D. Dastan, D. Wang, H. Garmestani, X.M. Wang, S. Talu, *J. Alloys Comp.* **805**, 229 (2019).

[18] N. Ghobadi, S. Rezaee, *J. Mater. Sci. Mater. Electron.* **27**, 8464 (2016).

[19] S. Stach, W. Sapota, Ş. Ţălu, A. Ahmadpourian, C. Luna, N. Ghobadi, A. Arman, M. Ganji, *J. Mater. Sci. Mater. Electron.* **28**, 2113 (2017).

[20] P. Kaspar, D. Sobola, R. Dallaev, S. Ramazanov, A. Nebojsa, S. Rezaee, L. Grmela, *Appl. Surf. Sci.* **493**, 673 (2019).

[21] X. Zhu, J. Yang, D. Dastan, H. Garmestani, R. Fan, Z. Shi, *Composites Part A* **125**, 105521 (2019).

[22] A.G. Korpi, Ş. Ţălu, M. Bramowicz, A. Arman, S. Kulesza, B. Pszczolkowski, S. Jurecka, M. Mardani, C. Luna, P. Balashabadi, S. Rezaee, S. Gopikishan, *Mater. Res. Expr.* **6**, 086463 (2019).

[23] S. Rezaee, N. Ghobadi, *Res. Phys.* **9**, 1148 (2018).

[24] H. Klung, L. Alexander, *X-ray Diffraction Procedure*, Wiley, New York 1974.

[25] D. Dastan, N. Chaure, M. Kartha, *J. Mater. Sci. Mater. Electron.* **28**, 7784 (2017).

[26] A. Ahmadpourian, C. Luna, A. Boochani, A. Arman, A. Achour, S. Rezaee, S. Naderi, *Eur. Phys. J. Plus* **131**, 381 (2016).

[27] D. Dastan, S.L. Panahi, N. Chaure, *J. Mater. Sci. Mater. Electron.* **27**, 12291 (2016).

[28] J.I. Langford, A.J. Wilson, *J. Appl. Crystallogr.* **11**, 102 (1978).

[29] T.C. Huang, G. Lim, F. Parmigiani, E. Kay, *J. Vac. Sci. Technol. A* **3**, 2161 (1985).

[30] M. Alijani, B.K. Kaleji, S. Rezaee, *Opt. Quant. Electron.* **49**, 225 (2017).

[31] A. Arman, Ş. Ţălu, C. Luna, A. Ahmadpourian, M. Naseri, M. Molamohammadi, *J. Mater. Sci. Mater. Electron.* **26**, 9630 (2015).

[32] Ş. Ţălu, S. Solaymani, M. Bramowicz, S. Kulesza, A. Ghaderi, S. Shahpouri, S.M. Elahi, *J. Mater. Sci. Mater. Electron.* **27**, 9272 (2016).

[33] Ş. Ţălu, S. Stach, S. Valedbagi, S.M. Elahi, R. Bavadi, *Mater. Sci. Poland* **33**, 137 (2015).

[34] N. Naseri, S. Solaymani, A. Ghaderi, M. Bramowicz, S. Kulesza, Ş. Ţălu, M. Pourreza, S. Ghasemi, *RSC Adv.* **7**, 12923 (2017).

[35] D. Sobola, Ş. Ţălu, S. Solaymani, L. Grmela, *Microsc. Res. Tech.* **80**, 1328 (2017).

[36] Ş. Ţălu, *Micro and Nanoscale Characterization of Three Dimensional Surfaces. Basics and Applications*, Napoca Star Publishing House, Cluj-Napoca 2015.

[37] Ş. Ţălu, S. Stach, A. Méndez, G. Trejo, M. Ţălu, *J. Electrochem. Soc.* **161**, D44 (2014).

[38] A.B. Chhabra, C. Meneveau, R.V. Jensen, K.R. Sreenivasan, *Phys. Rev. A* **40**, 5284 (1989).

[39] R.B.A. Nor Asma, P.A. Yuli, C.I. Mokhtar, *J. Appl. Sci.* **11**, 2053 (2011).